Atmos. Meas. Tech., 15, 3213–3222, 2022
https://doi.org/10.5194/amt-15-3213-2022

Atmospheric Measurement Techniques
Open Access

A phase separation inlet for droplets, ice residuals, and interstitial aerosol particles

Libby Koolik[1,2,3], Michael Roesch[1,4], Carmen Dameto de Espana[5], Christopher Nathan Rapp[5], Lesly J. Franco Deloya[1], Chuanyang Shen[1,6], A. Gannet Hallar[7,8], Ian B. McCubbin[8], and Daniel J. Cziczo[1,2,5]

[1]Department of Earth, Atmospheric, and Planetary Sciences, Massachusetts Institute of Technology, Cambridge, MA 02139, USA
[2]Department of Civil and Environmental Engineering, Massachusetts Institute of Technology, Cambridge, MA 02139, USA
[3]Department of Civil and Environmental Engineering, University of California Berkeley, Berkeley, CA 94720, USA
[4]Department of Environmental Systems Science, Swiss Federal Institute of Technology, ETH Zurich, Zurich 8092, Switzerland
[5]Department of Earth, Atmospheric and Planetary Sciences, Purdue University, West Lafayette, IN 47907, USA
[6]Department of Atmospheric and Oceanic Sciences, Peking University, Beijing 100871, China
[7]Department of Atmospheric Sciences, University of Utah, Salt Lake City, UT 84112, USA
[8]Storm Peak Laboratory, Desert Research Institute, Steamboat Springs, CO 80488, USA

Correspondence: Daniel J. Cziczo (djcziczo@purdue.edu)

Received: 3 February 2021 – Discussion started: 18 March 2021
Revised: 6 April 2022 – Accepted: 27 April 2022 – Published: 30 May 2022

Abstract. A new inlet for studying the aerosol particles and hydrometeor residuals that compose mixed-phase clouds – the phaSe seParation Inlet for Droplets icE residuals and inteRstitial aerosol particles (SPIDER) – is described here. SPIDER combines a large pumped counterflow virtual impactor (L-PCVI), a flow tube evaporation chamber, and a pumped counterflow virtual impactor (PCVI) to separate droplets, ice crystals ($\sim$ 3–25 µm), and interstitial aerosol particles for simultaneous sampling. Laboratory verification tests of each individual component and the composite SPIDER system were conducted. Transmission efficiency, evaporation, and ice crystals' survival were determined to show the capability of the system. The experiments show the SPIDER system can separate distinct cloud elements and interstitial aerosol particles for subsequent analysis. As a field instrument, SPIDER will help explore the properties of different cloud elements and interstitial aerosol particles in mixed-phase clouds.

1 Introduction

A mixed-phase cloud has both liquid and ice phases (Korolev et al., 2003; Shupe et al., 2006) with variable number density and mass ratios of liquid to ice particles. Mixed-phase clouds are important factors in aviation and climate (Lohmann, 2017; McCoy et al., 2016; Shupe et al., 2008). In aviation, supercooled droplets can cause aircraft icing and engine power loss (Strapp et al., 2016). In climate, the role clouds play in the earth's radiative budget remains uncertain (Boucher et al., 2013; McCoy et al., 2016). As aerosol particle concentration increases in the atmosphere, liquid clouds may have decreased droplet size and increased spatial and temporal extent (Boucher et al., 2013). This will change the radiative forcing at the top of the atmosphere (cloud albedo effect) as well as the lifetime of a cloud (lifetime effect) (Lohmann and Hoose, 2009; Storelvmo et al., 2008). Mixed-phase clouds are particularly complicated because the partitioning of phases is critical in assessing these effects (Hirst et al., 2001; Korolev et al., 2003, 2017; Shupe et al., 2006; Tan and Storelvmo, 2019). At present, these effects are difficult to parameterize in models due to a lack of observational data on formation, properties, and phase partitioning

Published by Copernicus Publications on behalf of the European Geosciences Union.

(Kamphus et al., 2010; Shupe et al., 2006). This has resulted in a global effort to study these clouds (Abel et al., 2014; Davis et al., 2007a; Hiranuma et al., 2016; Kupiszewski et al., 2015; Lohmann, 2017; Lowenthal et al., 2019; Mertes et al., 2007; Patade et al., 2016; Ramelli et al., 2021; Ruiz-Donoso et al., 2020; Schmidt et al., 2017).

The microphysical formation processes of water and ice clouds are generally understood. Droplets form when a critical supersaturation, described theoretically by the Köhler equation, is exceeded. At this supersaturation, aqueous droplets are the favored state, and particles that activate are termed cloud condensation nuclei (CCN) (Pruppacher and Klett, 1997). Ice nucleation is more complex. Ice can form homogeneously, via spontaneous nucleation of ice in a solution droplet, at temperatures below −40 °C (Heymsfield et al., 2017; Koop et al., 2000). At higher temperatures, ice forms heterogeneously through different pathways promoted by ice-nucleating particles (INPs) (Hoose and Möhler, 2012; Kanji et al., 2017). The specific properties that determine an effective INP remain poorly understood (Kanji et al., 2017).

There is also uncertainty regarding the existence of both liquid and solid water in the same environment. The accepted theory is the Wegener–Bergeron–Findeisen (WBF) process, whereby ice crystals, depending on the specific environmental temperature and humidity, grow at the expense of droplet evaporation due to thermodynamic instability (Korolev, 2007; Pruppacher and Klett, 1997). Ice crystals have a lower saturation vapor pressure than water droplets below 0 °C, so the presence of crystals will lower the water vapor content and cause the droplets to shrink or, given sufficient time, evaporate completely (Shupe et al., 2006; Storelvmo et al., 2008; Tsushima et al., 2006; Verheggen et al., 2007). This effect is often limited by the concentration of ice crystals in the cloud, since ice crystals are often more scarce in mixed-phase cloud than droplets (Verheggen et al., 2007).

In situ observations are required to understand the natural efficiency of INP and the microphysical processes of mixed-phase clouds. Several in situ experiments to characterize INP (Hartmann et al., 2020; Irish et al., 2019; Si et al., 2019) have occurred in the Arctic, where there is a prevalence of mixed-phase stratiform clouds (e.g., 41 % of the time in the study of Shupe et al., 2006). Another common research location has been the Jungfraujoch (Eriksen Hammer et al., 2018; Lacher et al., 2021), a mountain-top site in Switzerland, which has high cloud coverage (37 % of the time); the clouds are often mixed in phase (Kamphus et al., 2010; Verheggen et al., 2007).

Two of the fundamental questions surrounding mixed-phase cloud formation are as follows: (1) what is the ratio of ice to water in a cloud, and (2) what are the aerosol particles that act as the CCN or INPs? Currently, there are a variety of instruments that can estimate ice or water content of a cloud (Abel et al., 2014; Davis et al., 2007a, b; Korolev et al., 1998; Strapp et al., 2016); however, these instruments do not report information about the underlying INPs or CCN.

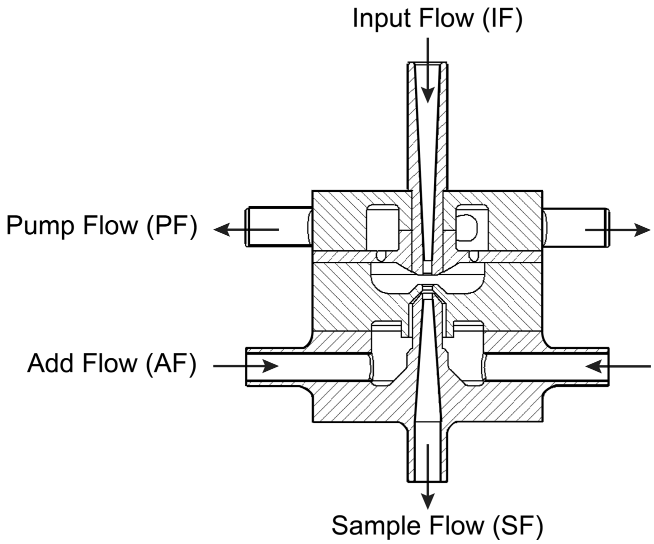

Figure 1. Cross-sectional view of the 3D-printed SPIDER PCVI with flows labeled. The 3D-printed PCVI features the improved conical input nozzle suggested by Kulkarni et al. (2011); otherwise, the design is the same as considered by Kulkarni et al. (2011).

One technique capable of separating ice and droplet residuals is the counterflow virtual impactor (CVI) and its laboratory counterpart, the pumped counterflow virtual impactor (PCVI). These methods use the property that activated droplets or ice crystals are significantly larger than unactivated, or interstitial, aerosol particles (Slowik et al., 2011). By separating based on mass, researchers can study differences between activated and interstitial aerosol particle. This technique has been used in a large number of studies since the mid-1980s when it was first described by Ogren et al. (1985).

The PCVI uses vacuum-pumped air to form a stagnation plane based on the design of the CVI (Boulter et al., 2006; Hiranuma et al., 2016). A schematic of the PCVI used in this study is shown in Fig. 1. A vacuum pump is used to provide the "pump flow" (PF), while pressurized air is introduced as an "add flow" (AF). AF has also been referred to as the "counterflow"; these terms are synonymous with AF used throughout this work. The "input flow" (IF) is at the entrance of the PCVI, and the "sample flow" (SF) is at the terminus (Boulter et al., 2006; Friedman et al., 2013). The "effective counterflow" (ECF) is the difference of AF and SF and counteracts the IF to create a stagnation plane that particles of sufficient inertia must cross to be entrained in the SF. The 50 % cut size or "D50" describes the number-averaged particle size of sufficient inertia to be transmitted through the PCVI with 50 % efficiency. The AF-to-IF ratio can be adjusted to change the D50, reducing or increasing the inertial barrier (Kulkarni et al., 2011; Slowik et al., 2011).

The performance of the PCVI has been considered by Boulter et al. (2006) and Kulkarni et al. (2011). A treatment of inadvertent transmission of particles smaller than the D50 as well as droplet and ice crystal breakup was considered by Pekour and Cziczo (2011). The PCVI has been used in conjunction with cloud chambers for several studies (Baustian et al., 2012; Friedman et al., 2013; Slowik et al., 2011). A recent advance is the ability to improve performance and cut costs by building a PCVI using three-dimensional (3D) stereolithography (SLA) printing (Koolik, 2017). 3D printing allows for rapid prototyping for complex devices (Jacobs, 1992), making the development of less expensive PCVIs possible. 3D printing mitigates costs, decreases build time, reduces misalignment, and allows for rapid and inexpensive tests of potential structural improvements (Koolik, 2017).

2 Instrument theory and design

The phaSe seParation Inlet for Droplets icE residuals and inteRstitial aerosol particles (SPIDER) is a vertically aligned inlet system with three distinct outlet channels for sampling interstitial (or "unactivated") aerosol particles, droplet residuals, and ice crystal residuals (Fig. 2). It is comprised of three main components: a large PCVI (L-PCVI), a droplet evaporation chamber, and a PCVI. The droplet evaporation chamber is actively cooled and lined with a series of sensors to provide real-time information on the temperature profile.

A 3D-printed L-PCVI was based on the design of the machined ice-selecting pumped counterflow virtual impactor (IS-PCVI) described by Hiranuma et al. (2016). The flow rates used in this work and those of Hiranuma et al. (2016) are shown in Table 1. To ensure that large droplets and ice crystals were transmitted without breakup, the maximum Weber number (N_{We}) was calculated for these flows as 0.3 (see Fig. S1 in the Supplement), which is less than the limit of 10 suggested for the onset of hydrometeor breakup. Details and model results are provided in the Supplement. The L-PCVI was tested over a range of flow conditions that resulted in different D50s (see Fig. S2). When operated with a $70\,\mathrm{L\,min^{-1}}$ IF and $7\,\mathrm{L\,min^{-1}}$ AF (AF-to-IF ratio of 0.1), the IS-PCVI has a D50 of $\sim 9\,\mu\mathrm{m}$ (Hiranuma et al., 2016). By operating the L-PCVI with an AF-to-IF ratio of ~ 0.25, for example, the D50 is estimated to be in the 10 to $18\,\mu\mathrm{m}$ range. Because droplets and ice crystals are typically $10\,\mu\mathrm{m}$ or larger (Kleinman et al., 2012; Pruppacher and Klett, 1997; Rogers and Yau, 1989), only these activated droplets and ice crystals greater than the L-PCVI lower cut size and smaller than the inlet cut size will enter SF. Interstitial aerosol and any droplets and/or ice crystals below the L-PCVI cut size will be stopped and transmitted into the PF.

Ice crystals and supercooled droplets that pass through the L-PCVI enter the droplet evaporation chamber, which utilizes the WBF process. The chamber can be bare or ice-coated and held at $-16\,^{\circ}\mathrm{C}$, where the difference in saturation vapor pressure between water and ice is at its maximum. With an ice coating, the chamber is, by definition, at ice saturation at $-16\,^{\circ}\mathrm{C}$ (i.e., ice crystals were stable while droplets evaporated). A bare chamber is subsaturated with respect to both ice and droplets but with a higher evaporation rate (i.e., more subsaturated) for the latter. As discussed in the next section, at ice saturation and $-16\,^{\circ}\mathrm{C}$, droplets smaller than $25\,\mu\mathrm{m}$ in diameter can be fully evaporated in the chamber, while ice crystals are able to maintain their initial size.

A PCVI is mounted below the droplet evaporation chamber. For this work a commercial-machined PCVI (Model

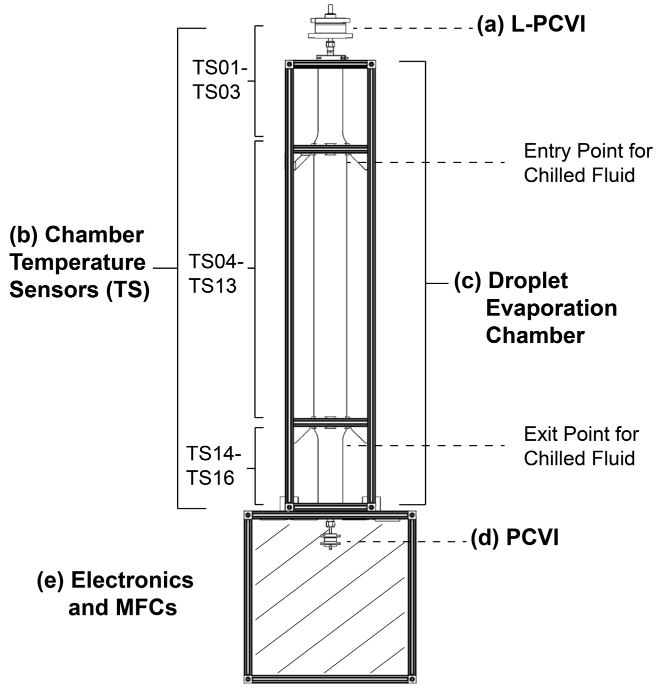

Figure 2. Schematic of SPIDER with its components labeled. **(a)** The L-PCVI (Hiranuma et al., 2016) separates interstitial aerosol from the droplets and ice crystals. **(b)** Thermocouples report the temperature in the chamber. **(c)** The chamber is cooled and held at ice saturation to evaporate droplets. **(d)** The PCVI downstream separates evaporated droplet residuals from ice crystals. **(e)** The bottom houses electronics and mass flow controllers (MFCs).

Table 1. L-PCVI flow tests.

SPIDER flow scenario	AF-to-IF ratio	Flows ($\mathrm{L\,min^{-1}}$)			
		AF	IF	PF	SF
N/A	0.14[a]	7.0	50.0		2.0
N/A	0.15[a]	11.5	75.0		2.5–6.0
N/A	0.16[a]	11.5	70.0		2.5–6.0
A	0.08[b]	7.0	86.5	87.0	6.5
B	0.11[b]	8.6	75.9	78.0	6.5
C	0.15[b]	6.6	44.9	45.0	6.5

[a] Ratios and flows used by Hiranuma et al. (2016); the PF was not provided by the authors as their SF was varied. [b] Ratios and flows used in this study. Flow scenario C was predominantly used in this work, although all three (A, B and C) were characterized.

8100, BMI Inc.), described by Boulter et al. (2006) and Kulkarni et al. (2011), and a 3D-printed PCVI, described by Koolik (2017), were both used, and their performance compared. As with the L-PCVI, the flow conditions in the PCVI determine the size selection cutoff. For the majority of tests described here, the PCVI flow rates used in SPIDER were PF, AF, and SF at 8.0, 2.5, and 1.0 $\mathrm{L\,min^{-1}}$, respectively. This results in a D50 of $\sim 5.2\,\mu\mathrm{m}$, which is used to reject evaporated droplet residuals and any inadvertently transmitted interstitial aerosol into the PF but admit ice crystals into the SF. Additional flow scenarios have been tested and summarized in Boulter et al. (2006), Kulkarni et al. (2011), and Koolik (2017). The aforementioned maximum N_{We} estimates for the PCVI are also less than 10 (see Fig. S3), suggesting that ice crystals are not subject to breakup in the PCVI under these conditions.

As noted, the flows in the L-PCVI set the lower size limit of droplets and/or ice transmitted into the SF. When operating SPIDER in the field, it is expected that an additional inlet will be added at the top of the series to prevent inadvertent transmission of debris or snow. In the case of the studies detailed in the following sections, it is assumed that a facility inlet from which SPIDER will sample sets the upper droplet and ice crystal size range. For this work, we base flows on the Desert Research Institute's Storm Peak Laboratory (SPL) inlet, described by Petersen et al. (2019). The SPL facility inlet has an upper D50 of $13\,\mu\mathrm{m}$ aerodynamic diameter with a broad cut size: 75 % of particles over $8\,\mu\mathrm{m}$ and 25 % of particles over $15\,\mu\mathrm{m}$ diameter are transmitted. Note that this transmission considers spherical particles of unit density (i.e., equivalent to water droplets); ice crystals of larger physical size are transmitted due to their lower density (Petersen et al., 2019).

Using this methodology, SPIDER offers simultaneous sampling channels for interstitial aerosol particles, droplet residuals, and ice crystal residuals via the PF of the L-PCVI, PF of the PCVI, and the SF of the PCVI, respectively.

3 Methodology

3.1 3D component fabrication

SPIDER incorporates a number of parts that were 3D-printed. SLA printing involves the photopolymerization of a liquid resin by a laser in a layer-by-layer process. This printing method was chosen for resolution, surface quality, low shrinkage, and low distortion (Bartolo, 2011; Bhushan and Caspers, 2017; Hagiwara, 2004). There are drawbacks and common errors that occur with SLA, including overcuring (solidified material fails to bind with the layer below it) and time-intensive post-processing (Jacobs, 1992; Wong and Hernandez, 2012); parts with these errors were rejected before use. The printer used for SPIDER components (Form 2, Formlabs Inc.) uses a 405 nm laser to cure specific coordinates in a resin bath to create the part in a layered structure (3D Printing with Desktop Stereolithography, 2020). Parts for SPIDER were printed from tough resin (FLTOTL03, Formlabs Inc.) with $100\,\mu\mathrm{m}$ layer resolution. After prints were completed, the parts were post-processed following the procedure described by Roesch et al. (2017) and Rösch and Cziczo (2020).

3.2 Instrumentation

Two particle sizing instruments were used for SPIDER performance testing, calibration, and data acquisition: an optical particle sizer (OPS; TSI, Model 3330) with an optical sizing range from 0.3 to $10\,\mu\mathrm{m}$ with a total flow rate of $1.0\,\mathrm{L\,min^{-1}}$ and an aerodynamic particle sizer (APS; TSI, Model 3321) with an optical sizing range from 0.3 to $20\,\mu\mathrm{m}$ with a total flow rate of $5.0\,\mathrm{L\,min^{-1}}$.

The evaporation chamber was cooled using a low-temperature cooling bath (Proline RP 1290, Lauda-Koenigshofen). Additional specifications and the operating procedure for SPIDER are included in the Supplement.

4 Validation experiments

In order to validate the SPIDER method, individual components were tested in the laboratory to determine performance and/or for comparison to previous studies. Droplets or ice crystals were then sent through the complete SPIDER setup to determine transmission, evaporation/sublimation, and rejection efficiency of each phase.

4.1 L-PCVI

Hiranuma et al. (2016) described the expected working conditions of the IS-PCVI, the design basis for the L-PCVI, at different flow ratios. For this work, the performance of the L-PCVI was investigated using solid soda lime glass microspheres (Cospheric LLC, $\rho = 2.5\,\mathrm{g\,cm^{-3}}$) with a diameter distribution of 1 to $50\,\mu\mathrm{m}$. A size distribution of the soda lime glass microspheres is presented in Fig. 3. Aerosol particles were generated with a multi-wrist shaker (Lab-Line Multi-wrist Shaker, Model 3589). A 500 mL Erlenmeyer flask containing the microspheres was attached to the shaker. Aerosol particles were suspended by injecting $5\,\mathrm{L\,min^{-1}}$ filtered air into the top of the flask and setting the wrist to ~ 750 rpm. The resulting aerosol into one leg of a Y was attached to the top of the L-PCVI. The other leg of the Y was attached to a HEPA filter to balance the flows in the system with particle-free air. Additional flows through the L-PCVI were controlled with mass flow controllers (Alicat Scientific, Inc.). The particle size distribution at the outlet of the L-PCVI was monitored with the APS. The SF of the L-PCVI was typically fixed at $\sim 6.5\,\mathrm{L\,min^{-1}}$ with the APS sampling at $1\,\mathrm{L\,min^{-1}}$ and the remaining $\sim 5.5\,\mathrm{L\,min^{-1}}$ exhausted through a filter.

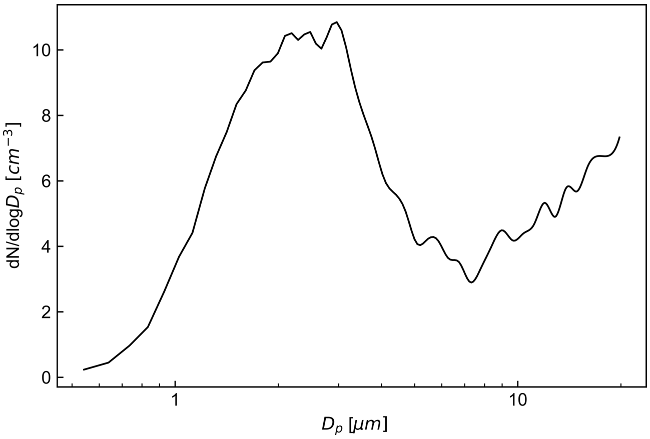

Figure 3. Number concentration as a function of the aerodynamic particle diameter of soda lime glass microspheres used for L-PCVI and SPIDER validation experiments.

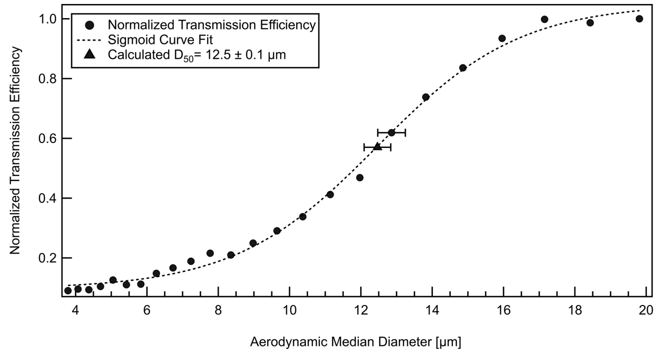

Figure 4. Transmission efficiency from the L-PCVI as a function of particle aerodynamic diameter (solid circles) fit with a sigmoid (solid line). The triangle represents the size at which 50 % of particles are transmitted (the experimental D50). The representative error, ±3 %, due to instrument uncertainty, is shown on a point close to the D50 and on the D50.

The L-PCVI transmission efficiency is defined as the ratio of particle number concentration of the SF to particle number concentration of the IF as a function of the aerodynamic diameter and the product of the enhancement factor (EF). The EF is defined as the ratio of the IF to the SF, the enhancement of particle concentration inherent to a CVI. The transmission efficiency of the L-PCVI was determined by comparing the aerosol size distributions with and without the PF and AF operating. Figure 4 shows the transmission efficiency corresponding to the flow configuration with a constant PF of 45 L min^{-1} and AF of 6.6 L min^{-1} as a function of the aerodynamic diameter (i.e., scenario C in Table 1). The D50 was determined by fitting a sigmoid curve and was calculated under these flows to be 12.5 ± 0.1 µm. The D50 from experiments using different flows configuration can be characterized as a function of the AF-to-IF ratio, analogous to Hiranuma et al. (2016). This is represented in Fig. S2 and correlates linearly to the AF-to-IF ratio (correlation coefficient = 0.85).

4.2 Droplet evaporation chamber

4.2.1 Droplet experiments

Droplet evaporation was considered based on the equations in Lohmann et al. (2016). From the model (see Fig. S4), it is expected that droplets entering the chamber 12.5 µm in diameter or smaller will fully evaporate before reaching the PCVI for chamber supersaturation 0.9 and lower during the approximately 25 s residence time. Droplets between 12.5 and 25 µm diameter will evaporate if the chamber supersaturation is below 0.5. Droplets larger than 25 µm are expected to partially but not fully evaporate within the chamber; this sets an effective upper limit for SPIDER.

In practice, the supersaturation of the chamber and the L-PCVI AF determines the supersaturation droplets' experience. A static SPIDER at −16 °C with ice-coated walls has a supersaturation with respect to ice that is, by definition, 1 but 0.85 with respect to liquid water (i.e., the model suggests droplets somewhat larger than 12.5 µm in diameter will fully evaporate). Hygrometer measurements show that dry air from the L-PCVI AF reduces this to 0.75. At this lower supersaturation, the model suggests that droplets with a diameter 20 µm and smaller fully evaporated in the chamber.

The evaporation as a function of the residence time was tested with aqueous ammonium sulfate droplets. Droplets were generated with a bubble burst generator ("bubbler") containing 0.1 g mL^{-1} ammonium sulfate. An aerosol flow of 0.6 L min^{-1} was diluted with 0.4 L min^{-1} humidified filtered air to obtain a 1 L min^{-1} SF. This flow was introduced via a 0.5 cm diameter injector at different locations in the chamber to vary the residence time, and the size distribution was recorded with the OPS. The size distribution corresponding to each residence time is shown in Fig. 5. The size distribution of the shortest residence time (0.2 s) reflects the initial droplet size distribution. Due to the OPS size range, only particles smaller than 10 µm diameter can be directly measured, although the distribution reflects decreasing particle numbers larger than this size; a linear extrapolation of the size distribution suggests that particles up to 20 µm diameter may have been present in the flow. Longer residence times indicate droplet evaporation, with initially larger droplets becoming smaller and eventually falling below the instrumental size range. In the longest residence time case (28.5 s), droplets have evaporated below ∼ 2.5 µm diameter.

4.2.2 Ice crystal experiments

Ice crystals were passed through the evaporation chamber to validate transmission. Droplets were created using a bubbler containing 0.1 g mL^{-1} ammonium sulfate. A 1 L min^{-1} droplet flow was isokinetically injected at the center of a

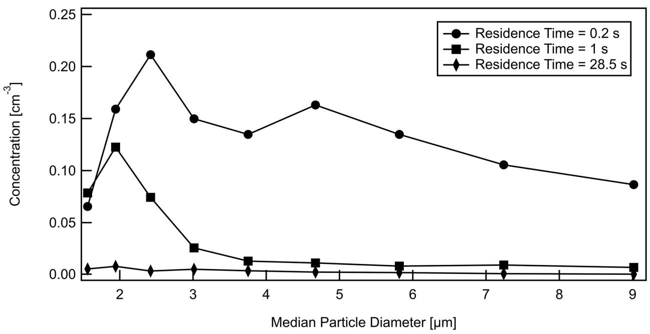

Figure 5. Droplet concentration at the outlet of the evaporation chamber as a function of the optical particle diameter for different residence times.

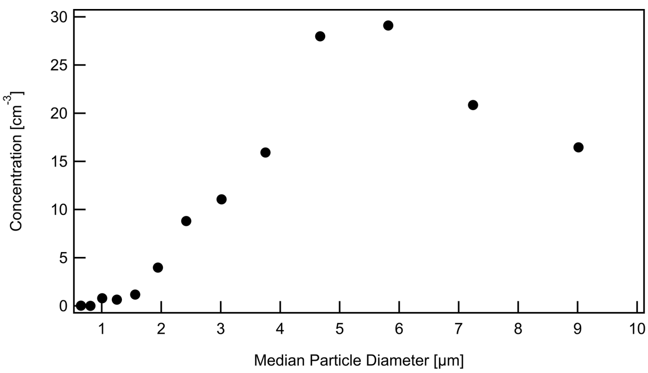

Figure 6. Ice crystals' concentration at the outlet of the evaporation chamber as a function of the optical particle diameter.

sheath air flow ($5\,\mathrm{L\,min^{-1}}$). The sheath air flow was cooled using liquid nitrogen introduced via a double concentric tube inlet. The low temperature caused homogeneous ice nucleation of the droplets. Based on observations with the OPS, a broad distribution of ice crystals was formed with a mode size centered between 5 and 6 µm diameter. The evaporation chamber and the outlet were cooled using the low temperature cooling bath set at $-16\,°\mathrm{C}$. A flow of $6\,\mathrm{L\,min^{-1}}$, consistent with the operational SPIDER flow (see Sect. 4.5), was injected at the top of the evaporation chamber. The size distribution at the bottom of evaporation chamber was determined with the OPS; the resulting size distribution (i.e. the size distribution of the sustained ice crystals) is represented in Fig. 6. No change in ice mode size or number concentration was observed. This was consistent with the evaporation calculations and indicated minimal or no sublimation of ice crystals under the SPIDER operating conditions.

4.3 PCVI

A validation of a 3D-printed PCVI was performed by Koolik (2017) following Boulter et al. (2006) and Kulkarni et al. (2011). Using a bubbler containing a solution of $0.1\,\mathrm{g\,L^{-1}}$ ammonium sulfate, measurements of D50 under various flow

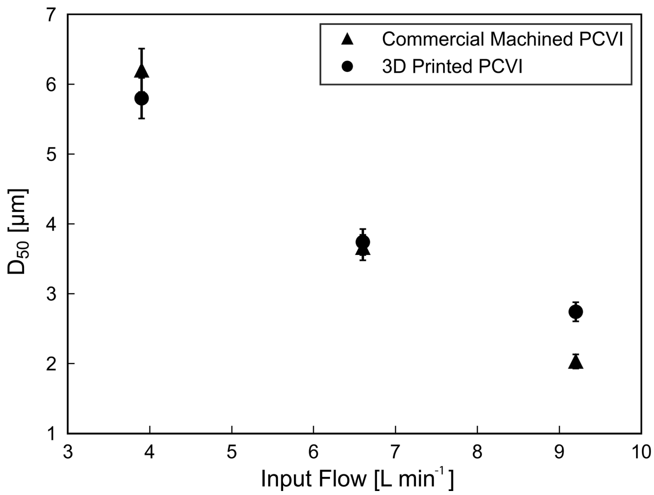

Figure 7. Comparison of D50 values for a commercial-machined and 3D-printed PCVI as a function of IF.

scenarios were performed and compared with the OPS. The size distribution of particles generated with the bubbler is represented in the Supplement (Fig. S5). With a constant AF of $2.5\,\mathrm{L\,min^{-1}}$ and SF of $1.0\,\mathrm{L\,min^{-1}}$, the 3D-printed PCVI had a working range of IF from 3.9 to $9.2\,\mathrm{L\,min^{-1}}$. The results of the comparison between the 3D-printed PCVI and the commercial-machined PCVI within this range are shown in Fig. 7.

Using the SPIDER PCVI flows mentioned in Sect. 2, a PCVI D50 of ~ 5 µm diameter is expected from the literature (Boulter et al., 2006; Kulkarni et al., 2011). To validate the D50, the SF from the PCVI was compared to the initial size distribution (i.e., for each size bin of OPS data). The transmission efficiency of each bin size was calculated and the data fit with a sigmoid; the D50 was defined as the particle diameter size that corresponded to 50 % of the maximum transmission efficiency on the sigmoid. An example of data using the SPIDER operational flows and the sigmoidal fit corresponding to a D50 of 5.1 ± 0.1 µm is shown in Fig. 8. The operational flows used in SPIDER are summarized in Sect. 2. Additional verification experiments are summarized in the Supplement (Fig. S6).

4.4 Composite SPIDER experiment

The composite SPIDER instrument, composed of the L-PCVI, the evaporation chamber, and the PCVI, was tested in the laboratory. The L-PCVI aerosol generation method, described in Sect. 4.1, was repeated. A $5\,\mathrm{L\,min^{-1}}$ aerosol flow was combined with filtered air. The PF and the AF used in the L-PCVI were 45 and $6.6\,\mathrm{L\,min^{-1}}$ respectively. The SF of the L-PCVI, $6.5\,\mathrm{L\,min^{-1}}$, corresponded to the flow through the evaporation chamber and the IF of the PCVI. The PCVI PF and AF in this case were 7 and $1.5\,\mathrm{L\,min^{-1}}$, respectively. While the flow conditions for the PCVI in this test are not

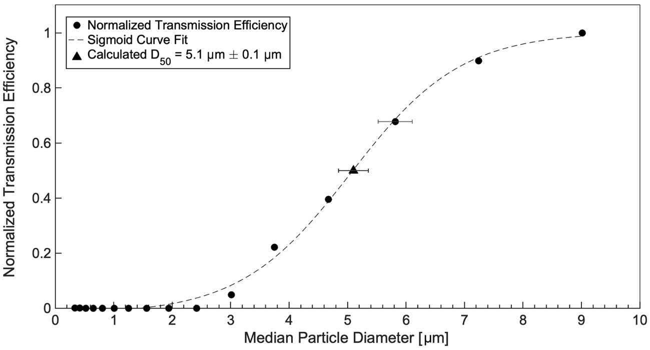

Figure 8. Transmission efficiency from the PCVI as a function of particle diameter (solid circles) fit with a sigmoid (dashed line). The triangle represents the size at which 50 % of particles are transmitted (the experimental D50). The representative error, ±5 % due to instrument uncertainty as specified by the manufacturer, is shown on a point close to the D50 and on the D50.

identical to the flows tested in Sect. 4.4, this flow scenario is consistent with the working range of flows in the 3D-printed PCVI. In order to determine the overall transmission efficiency (TE) of the system, the size distribution at the outlet was determined with the OPS. First, both AFs and PFs were turned off to obtain the initial size distribution, including any losses in the evaporation chamber and connections. All flows were then set to determine the size distribution at the outlet. The TE in this case was calculated as the ratio of the concentration when flows are turned on to the concentration when flows are turned off as a function of the optical size. The TE is then normalized through division by the product of the enhancement factor of the L-PCVI and the PCVI. The normalized TE as a function of particle diameter is presented in Fig. 9. Similar to the L-PCVI and PCVI, a sigmoid function was fit to obtain the cutoff size. The D50 for the combined system was 4.8 ± 0.1 µm.

5 Conclusion and future work

Laboratory studies have been used to show that both the individual components and composite SPIDER worked as designed.

In the verification experiments, each component of SPIDER was isolated and tested to validate that it performed its role in the overall system. Comparisons, when possible, were made with previous studies. Once each component was verified individually, a test was done to ensure that the combination also functioned using either microbeads or a combination of droplets and ice crystals. Multiple experiments with different flow combinations were performed to obtain the D50 as a function of the AF-to-IF ratio for both the L-PCVI and PCVI. This allowed for determination of a SF for the L-PCVI that was simultaneously suitable for droplet evaporation and as a viable IF for the PCVI.

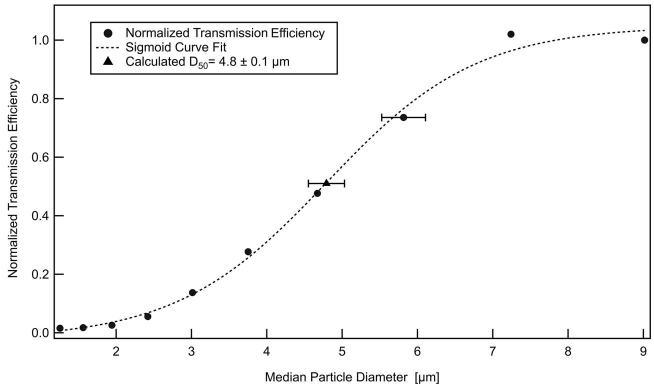

Figure 9. Transmission efficiency from SPIDER as a function of particle aerodynamic diameter (solid circles) fit with a sigmoid (solid line). The triangle represents the size at which 50 % of particles are transmitted (the experimental D50). The representative error, ±5 %, due to instrument uncertainty, is shown on a point close to the D50 and on the D50. Note that the SPIDER transmission efficiency represents the sequential transmission of the L-PCVI and PCVI.

Hiranuma et al. (2016) showed that the D50 linearly correlates with the AF-to-IF ratio (coefficient, $r = 0.85$). Our experimental results of the D50 as a function of the AF-to-IF ratio are somewhat lower than the experimental results from Hiranuma et al. (2016), although we note the difference in 3D-printed and machined L-PCVIs and somewhat different inlet and outlet designs and lengths described previously.

The PCVI was calibrated to define the working flows and to determine its the transmission efficiency. The obtained D50 is ~ 5 µm, similar to results from previous studies (Boulter et al., 2006; Kulkarni et al., 2011). The commercial-machined PCVI and the 3D-printed PCVI were calibrated and compared and are in good agreement.

The goal of this work was to develop an inlet system for separation and subsequent sampling of interstitial aerosol and cloud elements in mixed-phase clouds. Through these laboratory verification tests we have demonstrated that SPIDER is capable of sorting the three components of mixed-phase clouds into distinct channels.

It should be noted that there is not necessarily a one-to-one relationship between droplets and ice crystals and residuals. Droplets or ice crystals can scavenge gas- and particle-phase constituents. Droplets and ice crystals can also undergo breakup or secondary formation processes. The purpose of this work is to detail a means for separation of interstitial aerosol, droplets, and ice crystals into three separate channels. The specific cloud properties, such as cloud lifetime, scavenging rates, breakup processes, and secondary hydrometeor production mechanisms, at a sampling site will dictate the efficacy of SPIDER to resolve residuals.

Future goals include coupling SPIDER to a particle mass spectrometer in order to determine chemical composition of interstitial aerosol, droplet, and ice residuals within mixed-phase clouds to allow for a determination of the differences between particles that nucleate droplets or ice from unactivated particles. Ultimately, information on cloud nucleation capabilities of various aerosol particles could be compared to laboratory work and integrated into climate models (Korolev et al., 2017; McCoy et al., 2016; Shupe et al., 2008).

Data availability. Datasets generated during the validation experiments are available as a public repository (Koolik et al., 2022a). All code written in support of this work is publicly available as Koolik et al. (2022b).

Supplement. The supplement related to this article is available online at: https://doi.org/10.5194/amt-15-3213-2022-supplement.

Author contributions. MR and DJC conceptualized the SPIDER inlet configuration. LK, MR, and CDdE designed the experiments, and LK, MR, CDdE, CNR, LJFD, AGH, IBM, and CS carried them out. LK, MR, and CNR developed analysis code, LK developed model code, and LK and CDdE performed data analysis and evaluation. LK, DJC, and CDdE prepared the manuscript with contributions from all co-authors.

Competing interests. The contact author has declared that neither they nor their co-authors have any competing interests.

Disclaimer. Publisher's note: Copernicus Publications remains neutral with regard to jurisdictional claims in published maps and institutional affiliations.

Acknowledgements. We would like to thank the William and Kumi Martin Foundation and the National Science Foundation for funding. Libby Koolik would like to thank the MIT Department of Civil and Environmental Engineering for providing fellowship funding. We further thank DMT for the SP2-XR and NASA for the APS used for characterization of the L-PCVI.

Financial support. This research has been supported by the National Science Foundation, Directorate for Geosciences (grant nos. 1749851 and 2054847).

Review statement. This paper was edited by Paolo Laj and reviewed by three anonymous referees.

References

3D Printing with Desktop Stereolithography: An Introduction for Professional Users, https://archive-media.formlabs.com/upload/Intro-sla-whitepaper-04.pdf, last access: 9 August 2020.

Abel, S. J., Cotton, R. J., Barrett, P. A., and Vance, A. K.: A comparison of ice water content measurement techniques on the FAAM BAe-146 aircraft, Atmos. Meas. Tech., 7, 3007–3022, https://doi.org/10.5194/amt-7-3007-2014, 2014.

Bartolo, P. J. (Ed.): Stereolithography: Materials, Processes, and Applications, Springer US, 340 pp., https://doi.org/10.1007/978-0-387-92904-0, 2011.

Baustian, K. J., Cziczo, D. J., Wise, M. E., Pratt, K. A., Kulkarni, G., Hallar, A. G., and Tolbert, M. A.: Importance of aerosol particle composition, mixing state, and morphology for heterogeneous ice nucleation: A combined field and laboratory approach, J. Geophys. Res., 117, D06217, https://doi.org/10.1029/2011JD016784, 2012.

Bhushan, B. and Caspers, M.: An overview of additive manufacturing (3D printing) for microfabrication, Microsyst. Technol., 23, 1117–1124, https://doi.org/10.1007/s00542-017-3342-8, 2017.

Boucher, O., Randall, D., Artaxo, P., Bretherton, C., Feingold, G., Forster, P., Kerminen, V.-M., Kondo, Y., Liao, H., Lohmann, U., Rasch, P., Satheesh, S. K., Sherwood, S., Stevens, B., and Zhang, X. Y.: Clouds and Aerosols, in: Climate Change 2013: The Physical Science Basis. Contribution of Working Group I to the Fifth Assessment Report of the Intergovernmental Panel on Climate Change, edited by: Stocker, T. F., Qin, D., Plattner, G. K., Tignor, M., Allen, S. K., Boschung, J., Nauels, A., Xia, Y., Bex, V., and Midgley, P. M., Cambridge University Press, Cambridge, United Kingdom and New York, NY, United States, 571–657, ISBN: 978-1-107-05799-1, 2013.

Boulter, J. E., Cziczo, D. J., Middlebrook, A. M., Thomson, D. S., and Murphy, D. M.: Design and performance of a pumped counterflow virtual impactor, Aerosol Sci. Tech., 40, 969–976, https://doi.org/10.1080/02786820600840984, 2006.

Davis, S. M., Avallone, L. M., Weinstock, E. M., Twohy, C. H., Smith, J. B., and Kok, G. L.: Comparisons of in situ measurements of cirrus cloud ice water content, J. Geophys. Res., 112, D10212, https://doi.org/10.1029/2006JD008214, 2007a.

Davis, S. M., Hallar, A. G., Avallone, L. M., and Engblom, W.: Measurement of total water with a tunable diode laser hygrometer: Inlet analysis, calibration procedure, and ice water content determination, J. Atmos. Ocean Tech., 24, 463–475, https://doi.org/10.1175/JTECH1975.1, 2007b.

Eriksen Hammer, S., Mertes, S., Schneider, J., Ebert, M., Kandler, K., and Weinbruch, S.: Composition of ice particle residuals in mixed-phase clouds at Jungfraujoch (Switzerland): enrichment and depletion of particle groups relative to total aerosol, Atmos. Chem. Phys., 18, 13987–14003, https://doi.org/10.5194/acp-18-13987-2018, 2018.

Friedman, B., Ardon-Dryer, K., Carrasquillo, A., Daumit, K., Boulanger, K., Cross, E., Browne, E., Kroll, J., Thornton, J., and Cziczo, D.: CCN closure and composition analysis of droplet-forming aerosol particle, AIP Conf. Proc., 1527, 832–835, https://doi.org/10.1063/1.4803400, 2013.

Hagiwara, T.: Current status and future prospects of laser stereolithography, Proc. SPIE, 5662, 644–648, https://doi.org/10.1117/12.596757, 2004.

Hartmann, M., Adachi, K., Eppers, O., Haas, C., Herber, A., Holzinger, R., Hünerbein, A., Jäkel, E., Jentzsch, C., van Pinxteren, M., Wex, H., Willmes, S., and Stratmann, F.: Wintertime airborne measurements of ice nucleating particles in the high Arctic: a hint to a marine, biogenic source for ice nucleating particles, Geophys. Res. Lett., 47, e2020GL087770, https://doi.org/10.1029/2020GL087770, 2020.

Heymsfield, A. J., Krämer, M., Luebke, A., Brown, P., Cziczo, D. J., Franklin, C., Lawson, P., Lohmann, U., McFarquhar, G., Ulanowski, Z., and Van Tricht, K.: Cirrus Clouds, Meteor. Mon., 58, 2.1–2.26, https://doi.org/10.1175/amsmonographs-d-16-0010.1, 2017.

Hiranuma, N., Möhler, O., Kulkarni, G., Schnaiter, M., Vogt, S., Vochezer, P., Järvinen, E., Wagner, R., Bell, D. M., Wilson, J., Zelenyuk, A., and Cziczo, D. J.: Development and characterization of an ice-selecting pumped counterflow virtual impactor (IS-PCVI) to study ice crystal residuals, Atmos. Meas. Tech., 9, 3817–3836, https://doi.org/10.5194/amt-9-3817-2016, 2016.

Hirst, E., Kaye, P. H., Greenaway, R. S., Field, P., and Johnson, D. W.: Discrimination of micrometre-sized ice and super-cooled droplets in mixed-phase cloud, Atmos. Environ., 35, 33–47, https://doi.org/10.1016/S1352-2310(00)00377-0, 2001.

Hoose, C. and Möhler, O.: Heterogeneous ice nucleation on atmospheric aerosols: a review of results from laboratory experiments, Atmos. Chem. Phys., 12, 9817–9854, https://doi.org/10.5194/acp-12-9817-2012, 2012.

Irish, V. E., Hanna, S. J., Willis, M. D., China, S., Thomas, J. L., Wentzell, J. J. B., Cirisan, A., Si, M., Leaitch, W. R., Murphy, J. G., Abbatt, J. P. D., Laskin, A., Girard, E., and Bertram, A. K.: Ice nucleating particles in the marine boundary layer in the Canadian Arctic during summer 2014, Atmos. Chem. Phys., 19, 1027–1039, https://doi.org/10.5194/acp-19-1027-2019, 2019.

Jacobs, P. F. (Ed.): Rapid Prototyping & Manufacturing: Fundamentals of Stereolithography, 1st edn., Society of Manufacturing Engineers, in cooperation with the computer and Automated Systems Association of SME, Dearborn, Michigan, United States, ISBN: 978-0-872-63425-1, 1992.

Kamphus, M., Ettner-Mahl, M., Klimach, T., Drewnick, F., Keller, L., Cziczo, D. J., Mertes, S., Borrmann, S., and Curtius, J.: Chemical composition of ambient aerosol, ice residues and cloud droplet residues in mixed-phase clouds: single particle analysis during the Cloud and Aerosol Characterization Experiment (CLACE 6), Atmos. Chem. Phys., 10, 8077–8095, https://doi.org/10.5194/acp-10-8077-2010, 2010.

Kanji, Z. A., Ladino, L. A., Wex, H., Boose, Y., Burkert-Kohn, M., Cziczo, D. J., and Krämer, M.: Overview of ice nucleating particles, Meteor. Mon., 58, 1.1–1.33, https://doi.org/10.1175/amsmonographs-d-16-0006.1, 2017.

Kleinman, L. I., Daum, P. H., Lee, Y.-N., Lewis, E. R., Sedlacek III, A. J., Senum, G. I., Springston, S. R., Wang, J., Hubbe, J., Jayne, J., Min, Q., Yum, S. S., and Allen, G.: Aerosol concentration and size distribution measured below, in, and above cloud from the DOE G-1 during VOCALS-REx, Atmos. Chem. Phys., 12, 207–223, https://doi.org/10.5194/acp-12-207-2012, 2012.

Koolik, L. P.: Characterization of a 3D printed pumped counterflow virtual impactor and an aerodynamic lens concentrator, BS thesis, Massachusetts Institute of Technology, Cambridge, Massachusetts, United States, http://hdl.handle.net/1721.1/114346 (last access: 23 May 2022), 2017.

Koolik, L., Roesch, M., Dameto de Espana, C., Rapp, C. N., Franco Deloya, L. J., Shen, C., Hallar, A. G., McCubbin, I. B., and Cziczo, D. J.: Replication Data for: A Phase Separation Inlet for Droplets, Ice Residuals, and Interstitial Aerosol Particles, Harvard Dataverse [data set], https://doi.org/10.7910/DVN/KVPXSB, 2022a.

Koolik, L., Roesch, M., Dameto de Espana, C., Rapp, C. N., Franco Deloya, L. J., Shen, C., Hallar, A. G., McCubbin, I. B., and Cziczo, D. J.: SPIDER Validation Scripts, Github [code], https://github.com/lkoolik/SPIDER_Validation, 2022b.

Koop, T., Luo, B., Athanasios, T., and Peter, T.: Water activity as the determinant for homogeneous ice nucleation in aqueous solutions, Nature, 406, 611–614, https://doi.org/10.1038/35020537, 2000.

Korolev, A.: Limitations of the Wegener–Bergeron–Findeisen mechanism in the evolution of mixed-phase clouds, J. Atmos. Sci., 64, 3372–3375, https://doi.org/10.1175/JAS4035.1, 2007.

Korolev, A., McFarquhar, G., Field, P. R., Franklin, C., Lawson, P., Wang, Z., Williams, E., Abel, S. J., Axisa, D., Borrmann, S., Crosier, J., Fugal, J., Krämer, M., Lohmann, U., Schlenczek, O., Schnaiter, M., and Wendisch, M.: Mixed-Phase Clouds: Progress and Challenges, Meteor. Mon., 58, 5.1–5.50, https://doi.org/10.1175/AMSMONOGRAPHS-D-17-0001.1, 2017.

Korolev, A. V., Strapp, J. W., Isaac, G. A., and Nevzorov, A. N.: The Nevzorov airborne hot-wire LWC–TWC probe: principle of operation and performance characteristics, J. Atmos. Ocean Tech., 15, 1495–1510, https://doi.org/10.1175/1520-0426(1998)015<1495:TNAHWL>2.0.CO;2, 1998.

Korolev, A. V., Isaac, G. A., Cober, S. G., Strapp, J. W., and Hallett, J.: Microphysical characterization of mixed-phase clouds, Q. J. Roy. Meteor. Soc., 129, 39–65, https://doi.org/10.1256/qj.01.204, 2003.

Kulkarni, G., Pekour, M., Afchine, A., Murphy, D. M., and Cziczo, D. J.: Comparison of experimental and numerical studies of the performance characteristics of a pumped counterflow virtual impactor, Aerosol Sci., Tech., 45, 382–392, https://doi.org/10.1080/02786826.2010.539291, 2011.

Kupiszewski, P., Weingartner, E., Vochezer, P., Schnaiter, M., Bigi, A., Gysel, M., Rosati, B., Toprak, E., Mertes, S., and Baltensperger, U.: The Ice Selective Inlet: a novel technique for exclusive extraction of pristine ice crystals in mixed-phase clouds, Atmos. Meas. Tech., 8, 3087–3106, https://doi.org/10.5194/amt-8-3087-2015, 2015.

Lacher, L., Clemen, H.-C., Shen, X., Mertes, S., Gysel-Beer, M., Moallemi, A., Steinbacher, M., Henne, S., Saathoff, H., Möhler, O., Höhler, K., Schiebel, T., Weber, D., Schrod, J., Schneider, J., and Kanji, Z. A.: Sources and nature of ice-nucleating particles in the free troposphere at Jungfraujoch in winter 2017, Atmos. Chem. Phys., 21, 16925–16953, https://doi.org/10.5194/acp-21-16925-2021, 2021.

Lohmann, U: Anthropogenic aerosol influences on mixed-phase clouds, Current Climate Change Reports, 3, 32–44, https://doi.org/10.1007/s40641-017-0059-9, 2017.

Lohmann, U. and Hoose, C.: Sensitivity studies of different aerosol indirect effects in mixed-phase clouds, Atmos. Chem. Phys., 9, 8917–8934, https://doi.org/10.5194/acp-9-8917-2009, 2009.

Lohmann, U., Lüönd, F., and Mahrt, F. (Eds.): An Introduction to Clouds: From the Microscale to Climate, Cambridge University Press, Cambridge, England, ISBN: 978-1-107-01822-8, 2016.

Lowenthal, D. H., Hallar, A. G., David, R. O., McCubbin, I. B., Borys, R. D., and Mace, G. G.: Mixed-phase orographic cloud microphysics during StormVEx and IFRACS, Atmos. Chem. Phys., 19, 5387–5401, https://doi.org/10.5194/acp-19-5387-2019, 2019.

McCoy, D. T., Tan, I., Hartmann, D. L., Zelinka, M. D., and Storelvmo, T.: On the relationships among cloud cover, mixed-phase partitioning, and planetary albedo in GCMs, J. Adv. Model. Earth Sy., 8, 650–668, https://doi.org/10.1002/2015MS000589, 2016.

Mertes, S., Verheggen, B., Walter, S., Connolly, P. J., Ebert, M., Schneider, J., Bower, K. N., Cozic, J., Weinbruch, S., Baltensperger, U., and Weingartner, E.: Counterflow virtual impactor based collection of small ice particles in mixed-phase clouds for the physico-chemical characterization of tropospheric ice nuclei: Sampler description and first case study, Aerosol Sci. Tech., 41, 848–864, https://doi.org/10.1080/02786820701501881, 2007.

Ogren, J. A., Heintzenberg, J., and Charlson, R. J.: In-situ sampling of clouds with a droplet to aerosol converter, Geophys. Res. Lett., 12, 121–124, https://doi.org/10.1029/GL012i003p00121, 1985.

Patade, S., Shete, S., Malap, N., Kulkarni, G., and Prabha, T. V.: Observational and simulated cloud microphysical features of rain formation in the mixed phase clouds observed during CAIPEEX, Atmos. Res., 169, 32–45, https://doi.org/10.1016/j.atmosres.2015.09.018, 2016.

Pekour, M. S. and Cziczo, D. J.: Wake capture, particle breakup, and other artifacts associated with counterflow virtual impaction, Aerosol Sci. Tech., 45, 758–764, https://doi.org/10.1080/02786826.2011.558942, 2011.

Petersen, R. C., Hallar, A. G., McCubbin, I. B., Ogren, J. A., Andrews, E., Lowenthal, D., Gorder, R., Purcell, R., Sleeth, D., and Novosselov, I.: Numerical, wind-tunnel, and atmospheric evaluation of a turbulent ground-based inlet sampling system, Aerosol Sci. Tech., 53, 712–727, https://doi.org/10.1080/02786826.2019.1602718, 2019.

Pruppacher, H. R. and Klett, J. D.: Microphysics of Clouds and Precipitation, 2nd edn., Springer Netherlands, Dordrecht, Netherlands, https://doi.org/10.1007/978-0-306-48100-0, 1997.

Ramelli, F., Henneberger, J., David, R. O., Lauber, A., Pasquier, J. T., Wieder, J., Bühl, J., Seifert, P., Engelmann, R., Hervo, M., and Lohmann, U.: Influence of low-level blocking and turbulence on the microphysics of a mixed-phase cloud in an inner-Alpine valley, Atmos. Chem. Phys., 21, 5151–5172, https://doi.org/10.5194/acp-21-5151-2021, 2021.

Roesch, M., Roesch, C., and Cziczo, D. J.: Dry particle generation with a 3-D printed fluidized bed generator, Atmos. Meas. Tech., 10, 1999–2007, https://doi.org/10.5194/amt-10-1999-2017, 2017.

Rogers, R. R. and Yau, M. K. (Eds.): A Short Course in Cloud Physics, 3rd edn., Butterworth Heinemann, Burlington, Massachusetts, ISBN: 978-0-080-57094-5, 1989.

Rösch, M. and Cziczo, D. J.: Aqueous particle generation with a 3D printed nebulizer, Atmos. Meas. Tech., 13, 6807–6812, https://doi.org/10.5194/amt-13-6807-2020, 2020.

Ruiz-Donoso, E., Ehrlich, A., Schäfer, M., Jäkel, E., Schemann, V., Crewell, S., Mech, M., Kulla, B. S., Kliesch, L.-L., Neuber, R., and Wendisch, M.: Small-scale structure of thermodynamic phase in Arctic mixed-phase clouds observed by airborne remote sensing during a cold air outbreak and a warm air advection event, Atmos. Chem. Phys., 20, 5487–5511, https://doi.org/10.5194/acp-20-5487-2020, 2020.

Schmidt, S., Schneider, J., Klimach, T., Mertes, S., Schenk, L. P., Kupiszewski, P., Curtius, J., and Borrmann, S.: Online single particle analysis of ice particle residuals from mountain-top mixed-phase clouds using laboratory derived particle type assignment, Atmos. Chem. Phys., 17, 575–594, https://doi.org/10.5194/acp-17-575-2017, 2017.

Shupe, M. D., Matrosov, S. Y., and Uttal, T.: Arctic mixed-phase cloud properties derived from surface-based sensors at SHEBA, J. Atmos. Sci., 63, 697–711, https://doi.org/10.1175/JAS3659.1, 2006.

Shupe, M. D., Daniel, J. S., de Boer, G., Eloranta, E. W., Kollias, P., Long, C. N., Luke, E. P., Turner, D. D., and Verlinde, J.: A focus on mixed-phase clouds, B. Am. Meteorol. Soc., 89, 1549–1562, https://doi.org/10.1175/2008BAMS2378.1, 2008.

Si, M., Evoy, E., Yun, J., Xi, Y., Hanna, S. J., Chivulescu, A., Rawlings, K., Veber, D., Platt, A., Kunkel, D., Hoor, P., Sharma, S., Leaitch, W. R., and Bertram, A. K.: Concentrations, composition, and sources of ice-nucleating particles in the Canadian High Arctic during spring 2016, Atmos. Chem. Phys., 19, 3007–3024, https://doi.org/10.5194/acp-19-3007-2019, 2019.

Slowik, J. G., Cziczo, D. J., and Abbatt, J. P. D.: Analysis of cloud condensation nuclei composition and growth kinetics using a pumped counterflow virtual impactor and aerosol mass spectrometer, Atmos. Meas. Tech., 4, 1677–1688, https://doi.org/10.5194/amt-4-1677-2011, 2011.

Storelvmo, T., Kristjansson, J. E., and Lohmann, U.: Aerosol influence on mixed-phase clouds in CAM-Oslo, J. Atmos. Sci., 65, 3214–3230, https://doi.org/10.1175/2008JAS2430.1, 2008.

Strapp, J. W., Lilie, L. E., Ratvasky, T. P., Davison, C. R., and Dumont, C.: Isokinetic TWC evaporator probe: development of the IKP2 and performance testing for the HAIC-HIWC Darwin 2014 and Cayenne-2015 field campaigns, in: 8th AIAA Atmospheric and Space Environments Conference, Washington, D. C., United States, 13–17 June 2016, https://doi.org/10.2514/6.2016-4059, 2016.

Tan, I. and Storelvmo, T.: Evidence of strong contributions from mixed-phase clouds to arctic climate change, Geophys. Res. Lett., 46, 2894–2902, https://doi.org/10.1029/2018GL081871, 2019.

Tsushima, Y., Emori, S., Ogura, T., Kimoto, M., Webb, M. J., Williams, K. D., Ringer, M. A., Soden, B. J., Li, B., and Andronova, N.: Importance of the mixed-phase cloud distribution in the control climate for assessing the response of clouds to carbon dioxide increase: a multi-model study, Clim. Dynam., 27, 113–126, https://doi.org/10.1007/s00382-006-0127-7, 2006.

Verheggen, B., Cozic, J., Weingartner, E., Bower, K., Mertes, S., Connolly, P., Gallagher, M., Flynn, M., Choularton, T., and Baltensperger, U.: Aerosol partitioning between the interstitial and the condensed phase in mixed-phase clouds, J. Geophys. Res., 112, D23202, https://doi.org/10.1029/2007JD008714, 2007.

Wong, K. V. and Hernandez, A.: A review of additive manufacturing, ISRN Mech. Eng., 2012, 208760, https://doi.org/10.5402/2012/208760, 2012.